



The mechanism of aqueous stress-corrosion cracking of $\alpha + \beta$ titanium alloys



Sheng Cao^{a,b,*}, Suming Zhu^a, Chao Voon Samuel Lim^c, Xigen Zhou^a, Xiaobo Chen^d,
Bruce R.W. Hinton^a, Rodney R. Boyer^e, James C. Williams^f, Xinhua Wu^{a,b}

^a Department of Materials Science and Engineering, Monash University, Clayton, VIC 3800, Australia

^b Monash Centre for Additive Manufacturing, 11-13 Normanby Road, Notting Hill, VIC 3168, Australia

^c Department of Chemical Engineering, Monash University, Clayton, VIC 3800, Australia

^d School of Engineering, RMIT University, Carlton, VIC 3053, Australia

^e RBTi Consulting, Bellevue, WA, United States

^f Department of Materials Science and Engineering, The Ohio State University, Columbus, OH 43210, United States

ARTICLE INFO

Keywords:

- A. Titanium
- B. SEM
- B. TEM
- C. Stress corrosion
- C. Hydrogen embrittlement

ABSTRACT

In a previous paper (Cao et al., 2017) [1], a transition in fracture mode in aqueous NaCl Stress-Corrosion Cracking (SCC) of Ti-8Al-1Mo-1 V was reported. This paper attempts to unravel the operating mechanism for SCC by dislocation analysis on the Focus Ion Beam (FIB) lift-out foils from pre-crack and the SCC regions. It is shown that both basal $\langle a \rangle$ and $\langle c + a \rangle$ slips are operative in the SCC region while the basal $\langle a \rangle$ is the only activated system in the pre-crack region. Moreover, there is an increase in dislocation density in the SCC region compared to the pre-crack region. Based on these observations, combined Absorption Induced Dislocation Emission (AIDE) and Hydrogen Enhanced Localized Plasticity (HELP) is proposed to be the operating mechanisms for SCC in $\alpha + \beta$ titanium alloys.

1. Introduction

Titanium (Ti) alloys are widely used in aerospace industry due to their high specific strength and corrosion resistance [2–5]. Ti-8Al-1Mo-1V (Ti-811) is a near α alloy, which is a subgroup of $\alpha + \beta$ Ti alloys [6]. It is composed of 8 Wt.% Al, 1 Wt.% Mo, 1 Wt.%V, and the base metal Ti. In aqueous sodium chloride (NaCl) solution with neutral pH, corrosion resistance of Ti-8Al-1Mo-1V is attributed to spontaneous passivation and the formation of an integrated, adherent, protective Ti oxide film [7]. However in stress-corrosion cracking (SCC), the passive oxide film at the crack tip is ruptured under mechanical load, which allows electrochemical reactions to occur. Anodic dissolution increased the Ti ion concentration in the solution at the crack tip, and the hydrolysis of titanium chloride produces a pH below 2 in neutral aqueous NaCl solutions [8–10].

For Ti and Ti alloys, α phase is the stable phase at low temperatures, and it has a hexagonal close packed (HCP) structure with limited slip systems. α phase transforms into β phase when the temperature is above the β/α allotropic transformation temperature. β phase has a body centered cubic (BCC) structure. The β -Ti volume varies depending on the alloying additions and processing/heat treatment temperatures.

The BCC β -Ti contains more operative slip systems in the β phase enabling more uniform deformation. Ti-811 is a near α Ti alloy having a small volume fraction of β phase (less than 10 vol.%) at room temperature and a high β transus temperature [2,3,11].

In addition to α and β phases, another important phase is the ordered α_2 . Precipitation of α_2 occurs within the α matrix at appropriate aging temperatures in Ti alloys containing more than 6 wt.% Al [2]. The SCC susceptibility is increased with Al and O additions, which is a result of more intense planar slip due to the ordering of Al and O elements [3,8,12]. Coherent and fine α_2 precipitates are sheared by moving dislocations, and then continuous slip can occur on the active slip plane, rather than initiating a new slip band on other planes. In a previous deformation investigation of Ti-6.6Al, dislocation glides were restricted to basal planes, which formed slip bands and destroyed α_2 precipitates [13], resulting in a greater dislocation density on a limited number of planes. Therefore, α_2 precipitates further localize the planar slip and can result in a more rapid SCC crack propagation.

In several previous studies of Ti-811 [8,14], quantitative tilt fractography studies of SCC facets determined that the fracture planes were inclined 5°–15° away from the basal plane, and some fracture planes were close to the generally found $\{10\bar{1}\}_\alpha$ hydride habit planes. Several

* Corresponding author at: Department of Materials Science and Engineering, Monash University, Clayton, Victoria 3800, Australia.
E-mail address: sheng.cao@monash.edu (S. Cao).

studies have suggested that SCC mechanisms in Ti alloys are related to either internal hydrogen or external absorbed hydrogen [10,15]. Internal hydrogen is solute hydrogen in the alloy, while external hydrogen is hydrogen absorbed as a result of cathodic electrochemical reactions at SCC crack tip [10,15].

A plausible SCC mechanism for Ti alloys is hydride formation and fracture mechanism, in which hydrides form at α/β interfaces and crack propagates along the grain boundary hydrides. However, there are two apparent differences. First, the hydride formation mechanism is kinetically sluggish. In a hydrogen embrittlement (HE) study of Ti-4Al, the first hydride formation took approximately 14 min (min) in an environment cell containing H_2 with pressure of 16 kPa [16]. In the K (stress intensity factor) independent region II, where the aqueous SCC crack propagation rate was as high as 10^{-5} m/s for Ti-8Al-1Mo-1V [1], it might be expected that this mechanism is not possible. Secondly, SCC fracture in Ti-811 is transgranular, while the hydride formation and fracture mechanism produces intergranular fracture [16,17]. Therefore, the hydride formation and fracture mechanism is not feasible for aqueous NaCl SCC of Ti-811.

Other possible SCC mechanisms are Absorption Induced Dislocation Emission (AIDE) and Hydrogen Enhanced Localized Plasticity (HELP) for non-hydride forming situations [10,15,18–22]. With AIDE, absorbed hydrogen weakens intermetallic bonding and facilitates dislocation emissions at a few surface atomic layers. In HELP, hydrogen concentration is high in the hydrostatic stress region around crack tip, and solute hydrogen interacts with dislocations and promotes dislocation movement. Both AIDE and HELP promote transgranular cracking, which is similar to transgranular SCC facets in near α Ti alloys [23]. The key difference between AIDE and HELP is whether hydrogen promotes dislocation emission or motion [10,15,18–21,24,25].

Although several hypotheses state that hydrogen is involved in the aqueous SCC of Ti-811 [8,10,15,18,19], there has been no evidence provided for the relationship between the microstructure, dislocation substructure, and the SCC mechanism for Ti-811. In the previous study [1], a fracture mode change from ductile dimples (pre-crack failure in air) to SCC facets (in aqueous NaCl solution) was observed. In order to help reveal the SCC mechanisms in Ti-811, this study investigated the differences in dislocation types and density associated with the dimples and facets, as well as how the SCC facets form in Ti-811. Focus Ion Beam (FIB) milling was used to extract a small volume of material beneath the fracture surface, and Transmission Electron Backscatter Diffraction (T-EBSD) and Transmission Electron Microscopy (TEM) were used to elucidate how the dimples and facets formed.

2. Experimental methods

Wrought Ti-811 and powder hot isostatically pressed (HIPed) Ti-811 were employed in this study. The wrought Ti-811 bar (diameter at 80 mm) with a duplex microstructure from Timet UK Limited was obtained for this study. The size range of α grains and colonies were 20–30 μm after a heat treatment at 860 °C for 30 min [1]. Pre-alloyed Ti-811 powders with a particle size ranging from 5 to 832 μm were provided by IMR, Chinese Academy of Science. 90% of these particles had a diameter less than 307 μm . These powders were encapsulated in mild steel cans and hot HIPed at 100 MPa, and 990 °C for four hours with a ramp rate of 5 °C/min. The powder HIPed Ti-811 had recrystallized α grains of 5–10 μm , and α laths with a thickness at 2 μm . The volume fraction of β phase was approximately 10% in both wrought Ti-811 and HIPed Ti-811. The concentrations of solute hydrogen in the wrought and HIPed Ti-811 were 34 and 24 ppm respectively based on the chemical analysis conducted by Luvak Laboratories Inc. (Boylston, MA, U.S). Double Cantilever Beam (DCB) specimens machined from the wrought and HIPed Ti-811 were used for the SCC test in a 0.1 M NaCl aqueous solution (pH at 5.7) at room temperature. The specimen potential was maintained at the open circuit potential and the NaCl solution was open to air. The crack length was

periodically measured by using scalpel to mark the crack front on both surfaces of the DCB specimens under an optical microscope [1].

All SCC fracture surfaces were examined by a FEI Quanta 3D FEG microscope. FIB was used to extract TEM foils from the pre-crack and SCC crack regions of wrought and HIPed Ti-811 samples. Those FIB lift-out foils were perpendicular to both the fracture surface and SCC crack propagation direction. In total, three FIB lift-out lamellae were prepared in this study. Regions 1 (lamella 1) and 2 (lamella 2) were sectioned from the dimpled and faceted fracture surfaces of wrought Ti-811, and another lamella 3 containing regions 3 and 4 was obtained from the faceted fracture surface of HIPed Ti-811 sample. For all lamellae, a 2.5 μm layer of platinum (Pt) was deposited on the fracture surface to reduce the ion beam damage. A sequentially reduced FIB energy was applied from the thinning to the polishing stages, and the final polish was conducted at 2 kV and 27 pA to remove a 40 nm thick layer of material.

Crystallographic orientations and Schmid factor calculations of all FIB foils were studied by using T-EBSD equipped with a FEI Quanta 3D FEG microscope at an accelerating voltage of 25 keV and electron current of 23 nA. The post data analysis was carried out by AZtecHLK and OIM™ software packages. In order to determine active slip systems, dislocation contrast experiments were performed based on a scalar product $g \cdot b$ invisibility criterion using a 200 keV FEI Tecnai G2 T20 TWIN TEM. A correlation between operating slip systems and the critical tensile stress was studied in the grains of interest based on Schmid's law.

3. Results

3.1. Fractography

The DCB samples were pre-loaded in air to a length of 3 mm on both side surfaces before immersing in the aqueous NaCl solution. Ductile dimples were found to be the characteristic fracture mode in the pre-crack region of the wrought Ti-811 condition (Fig. 1a). Fig. 1b shows a typical SCC fracture surface where a dimpled region was observed between transgranular facets indicated by the black arrowhead. The facets were formed at different heights, and their surfaces were covered by aligned ductile tear ridges. The size of facets was about 20 μm , which is similar to that of α grains in the wrought Ti-811 shown in previous work [1]. This suggests that the facets correspond to different α grains. Such a transgranular faceted fracture containing tear ridges is typical for SCC in $\alpha + \beta$ Ti alloys [8,14,26]. The observed fracture mode transition indicates a deformation mechanism change in the SCC.

Similar to the SCC facets of the wrought sample, the fracture characteristics are pre-crack dimples and SCC facets in the HIP-Ti-811 sample according to the previous study [1]. As shown in Fig. 1c, the SCC fracture surface of a HIPed Ti-811 sample also contained flat facets. These elongated facets corresponded to the size of lamellar microstructure in HIPed Ti-811 sample shown in the previous work [1]. Fig. 1d is a close up image of the white dashed line box in Fig. 1c. In addition to tear ridges, there were planar slip bands with spacing from 100 nm to 800 nm (features denoted by the white arrowhead) on the facet in Fig. 1d.

3.2. FIB lift-out and T-EBSD

FIB lift-out lamellae were obtained from the dimpled region of the pre-crack (Fig. 2b) of the wrought Ti-811 bar, and from the SCC fracture surfaces containing facets of the wrought and HIPed Ti-811 samples (Fig. 2e, and h). A small amount of Pt deposition maintained the foils after the final low FIB energy polishing at 2 kV and 27 nA to identify the fracture surface for the facet crystallography analysis. An interesting phenomenon was observed in region 2 of Fig. 2e, where a secondary crack was found at the top right corner of black dashed box, and both the secondary crack and main fracture surface were roughly

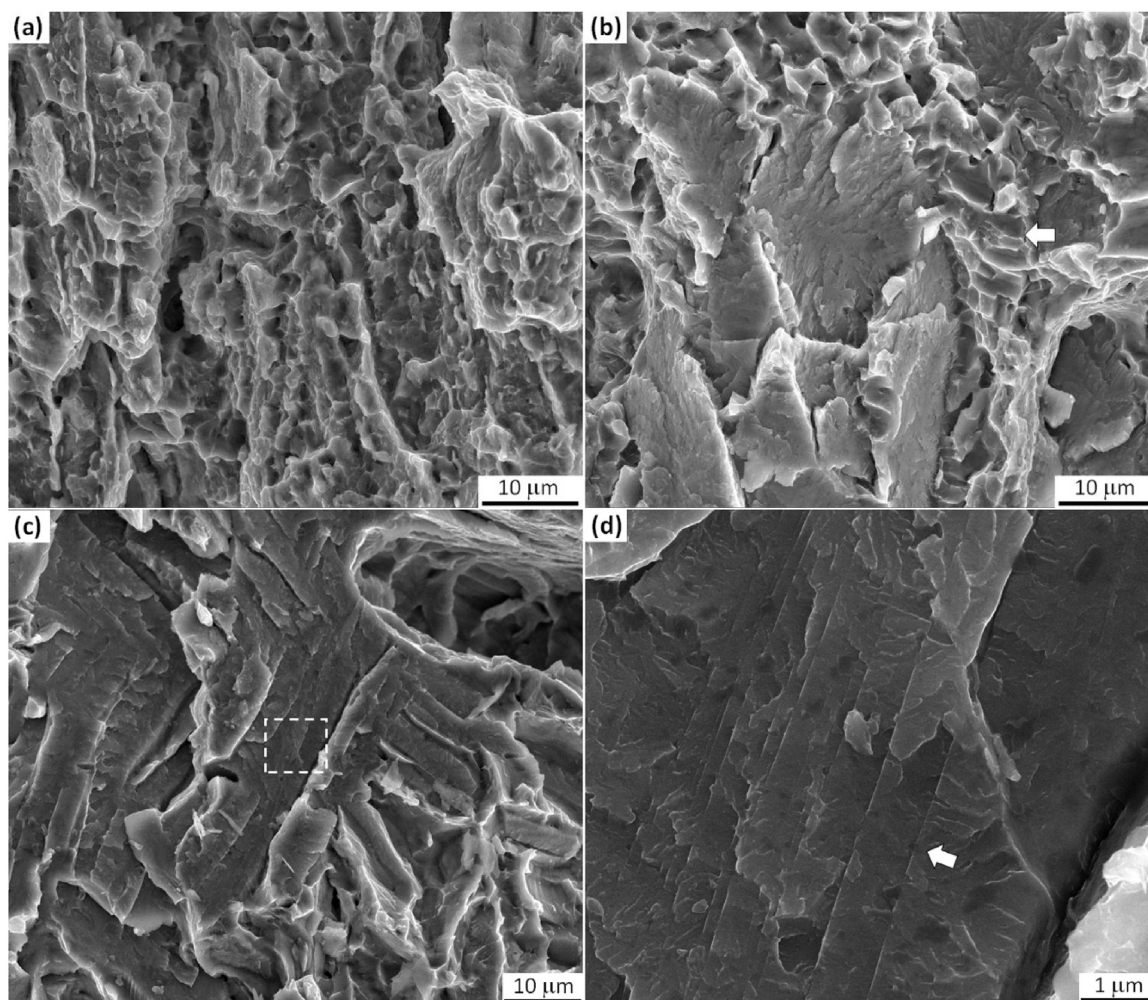


Fig. 1. Secondary electron images of fractography, (a) dimples on the pre-crack failed in air of a wrought Ti-811 sample, and (b) propagation SCC facets fractured in a 0.1 M aqueous NaCl solution of a wrought Ti-811 sample, a dimpled region is indicated by the white arrow; (c) propagation SCC facets fractured in a 0.1 M aqueous NaCl solution of a HIPed Ti-811 sample, and (d) localized slip band (the white arrowhead) observed on the SCC facets in the white dashed line box in (c).

parallel to the $(0001)_\alpha$ plane. Fig. 2h shows the foil sectioned from the faceted region of HIPed Ti-811, and the insert is an enlarged image of region 3. Stair-like steps were observed on the facets with a spacing of approximately 700 nm, which was expected as the planar slip bands similar to Fig. 1d.

The volume fraction of β phase was found to be about 10% in both wrought and HIPed Ti-811 based on the previous study [11], thus pole figures were only computed for α -Ti texture. With all the three lamellae, the loading condition was tensile stress along vertical direction (red arrows in Fig. 2b, e, and h). Fig. 2c is the pole figure of region 1 in Fig. 2b. There is a strong basal pole in the area of interest and the $[0001]_\alpha$ direction is inclined approximately 25° away from the tensile direction. For region 2 beneath facets (Fig. 2e), all the data points have their c -axis inclined approximate 45° away from the loading direction. As the size of α grains were in the range of 20–30 μm in the wrought Ti-811, the EBSD mapping area (black dashed box) of $2 \times 2 \mu\text{m}^2$ indicates that it could be a single grain in region 2, which agrees with the pole figure data. For region 3 beneath SCC facets of HIPed Ti-811 (Fig. 2h), the basal pole is approximately 6° away from the loading axis.

Based on the tensile loading direction (vertical direction in Fig. 2b, e, and h) and crystallographic orientations in the grains of interest, the relative critical tensile stress (σ_c) can then be calculated by the Schmid factor (m) and Critical Resolved Shear Stress (CRSS, τ_c) for various slip systems in α -Ti grains as following Eq. (1) [1]:

$$\sigma_c = \tau_c / m \quad (1)$$

The slip system with the lowest σ_c will be preferentially activated. As CRSS data for various slip systems in α phase of Ti-811 are not available, a reference relating to a Ti-6.6Al single crystal at 300 K was adopted considering its high Al content [13]. The combination of basal and prismatic $\langle a \rangle$ slip systems which gives a pyramidal $\langle a \rangle$ slip, was not considered here. The CRSS of $\langle c + a \rangle$ slip systems is roughly four times as high as that of $\langle a \rangle$ slip on either the basal or prismatic planes. Different types of $\langle c + a \rangle$ slip systems generally have not been listed clearly in numerous CRSS studies. Therefore, the same CRSS was used in our study for the first-order pyramidal $\{10\bar{1}1\}$ and second-order pyramidal $\{11\bar{2}2\} \langle c + a \rangle$ slip [27,28].

Table 1 lists the Schmid factors and relative σ_c of various slip systems in regions 1–3 as shown in Fig. 2. Although the α -Ti grain in region 1 is orientated such that $\langle c + a \rangle$ slip systems had the highest Schmid factor, the relative σ_c is still lower for basal $\langle a \rangle$ slip due to the high relative CRSS of $\langle c + a \rangle$ slip. Therefore, basal $\langle a \rangle$ slip is the easiest activated slip system compared to other systems in region 1. For region 2, the basal plane is inclined approximately 45° away from the loading axis, which means that the Schmid factor will be the highest for basal $\langle a \rangle$ slip, thus the basal $\langle a \rangle$ slip will be preferentially activated. In region 3, beneath the SCC facets of a HIPed Ti-811 sample, the c -axis is close to the stress axis which results in a high Schmid factor for pyramidal $\langle c + a \rangle$ slip systems, and a low relative σ_c in turn. However, the difference between the relative σ_c of $\langle c + a \rangle$ slip systems and basal $\langle a \rangle$ slip system is small, only about 20%. Unlike the other two regions (1 and 2) orientated favourably for basal $\langle a \rangle$ slip,

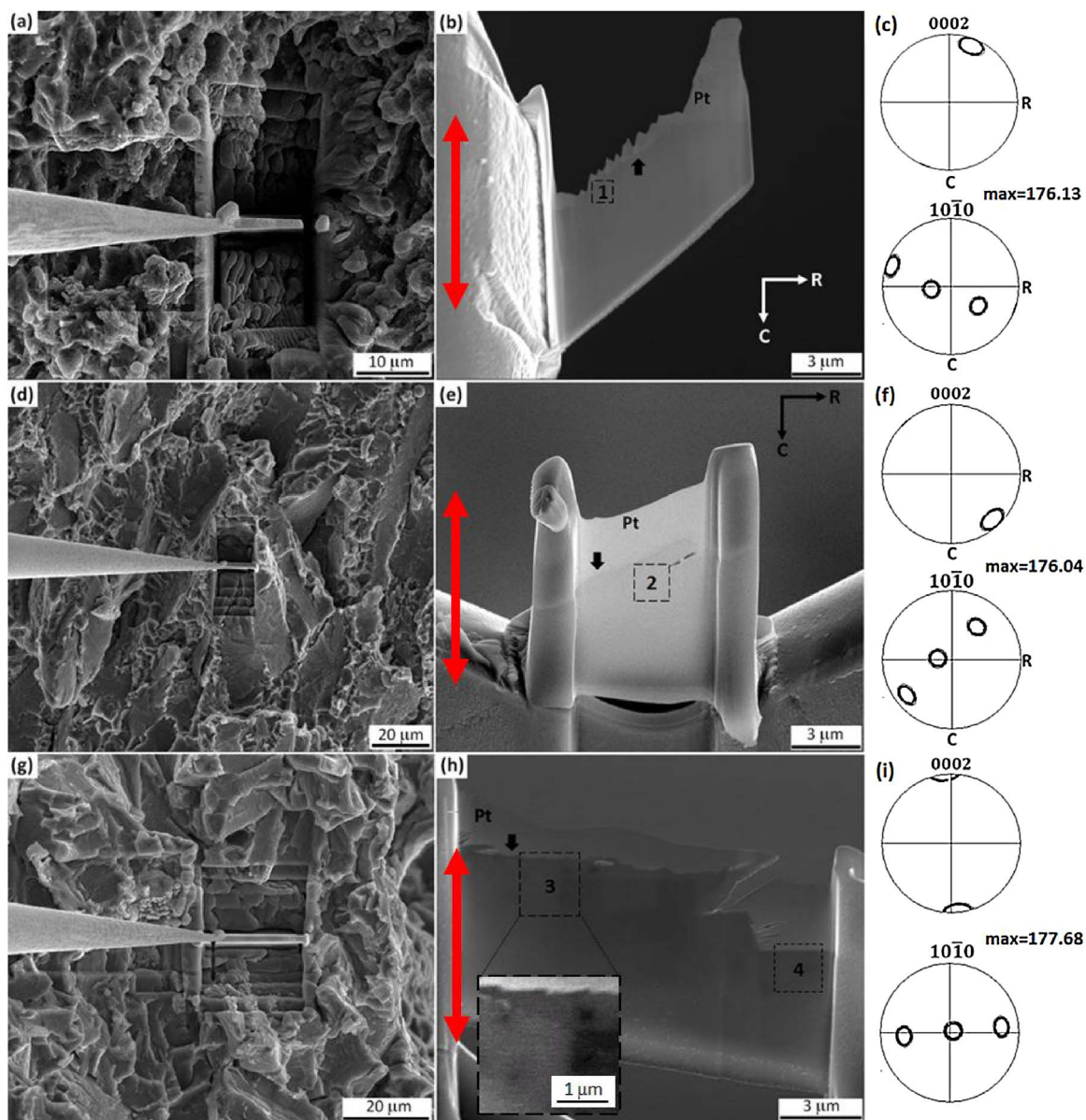


Fig. 2. (a-f) FIB lift-out lamellae obtained from a fractured wrought Ti-811 sample, (a) and (b) from pre-crack dimpled fracture, (d) and (e) from SCC faceted fracture. Pole figures of α phase, (c) the pole figure corresponding to region 1 in (b), (f) the pole figure corresponding to region 2 in (e). (g-i) FIB lift-out lamella obtained from a fractured HIPed Ti-811 sample, (g) and (h) from SCC faceted fracture, and the insert in (h) is an enlarged view of region 3; (i) the pole figure corresponding to region 3 in (h). All the fracture surfaces beneath the platinum (Pt) deposition are denoted by the black arrowheads in (b), (e) and (h).

Table 1
Schmid factors (m), relative CRSS (τ_c) and relative critical tensile stress (σ_c) for various slip systems for the regions of interest in the FIB lift-out lamellae in Fig. 2b, e and h.

	Slip systems*	Schmid Factor (m)	Relative CRSS (τ_c) [13]	Relative Critical tensile stress (σ_c)
Region 1: beneath the dimples in wrought Ti-811	$\langle a \rangle$	(0001) 0.368–0.369	0.2625	0.711–0.713
		{10 $\bar{1}$ 0} 0.076–0.077	0.2375	3.084–3.125
	$\langle c + a \rangle$	{10 $\bar{1}$ 1} 0.497–0.498	1	2.008–2.012
Region 2: beneath the SCC facets in wrought Ti-811	$\langle a \rangle$	{11 $\bar{2}$ 2} 0.463	1	2.16
		(0001) 0.493–0.500	0.2625	0.525–0.532
	$\langle c + a \rangle$	{10 $\bar{1}$ 0} 0.194–0.250	0.2375	0.950–1.224
Region 3: beneath the SCC facets in HIPed Ti-811	$\langle a \rangle$	{10 $\bar{1}$ 1} 0.345–0.411	1	2.433–2.899
		{11 $\bar{2}$ 2} 0.255–0.319	1	3.135–3.922
	$\langle c + a \rangle$	(0001) 0.075–0.109	0.2625	2.408–3.5
	{10 $\bar{1}$ 0} 0.003–0.007	0.2375	33.93–79.17	
	{10 $\bar{1}$ 1} 0.444–0.457	1	2.188–2.252	
	{11 $\bar{2}$ 2} 0.478–0.487	1	2.053–2.092	

* Where $\langle a \rangle$ -type slip systems have slip direction in $\langle 11\bar{2}0 \rangle$, and $\langle c + a \rangle$ -type slip direction is $\langle 11\bar{2}3 \rangle$.

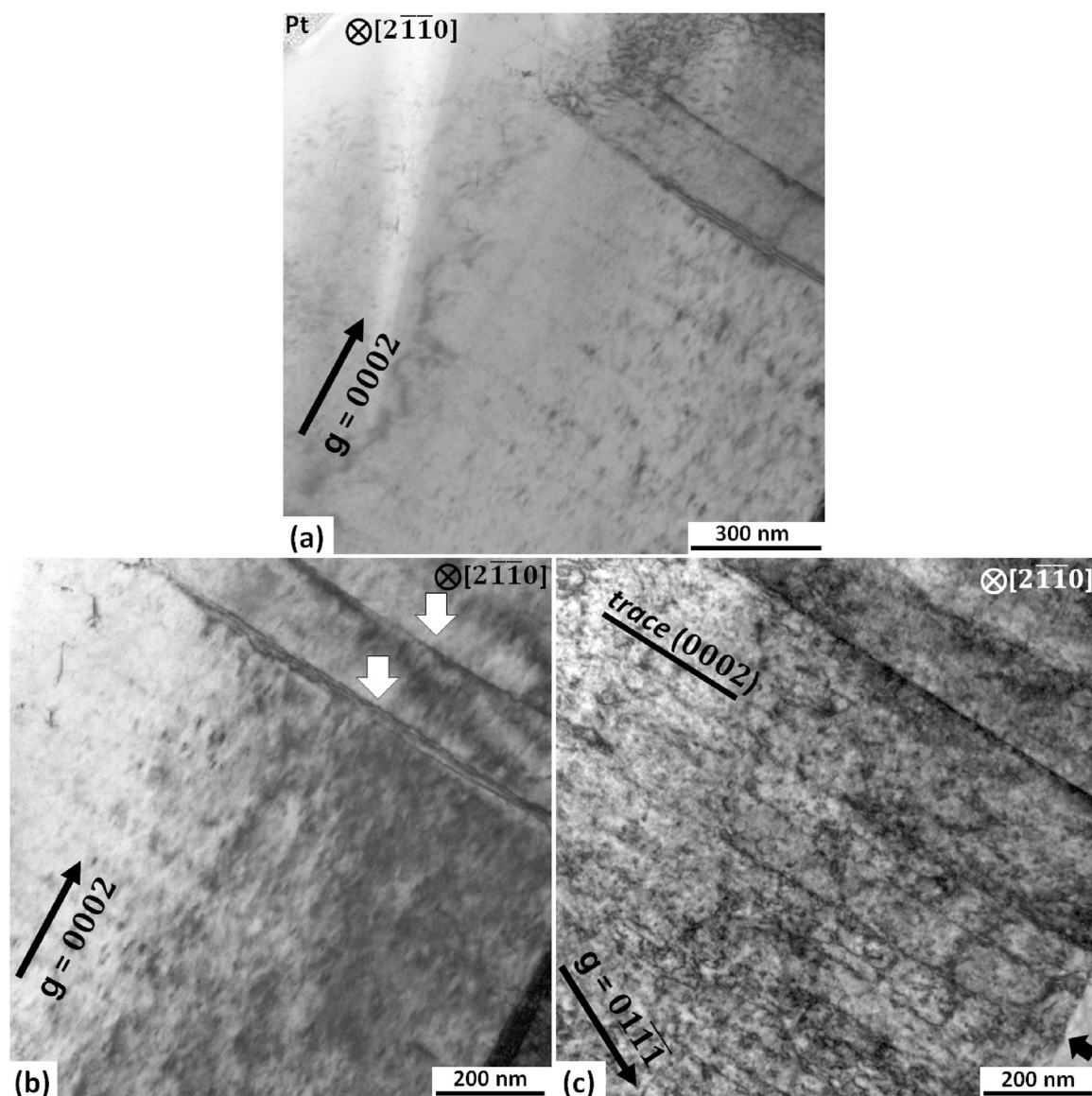


Fig. 3. Bright Field (BF) TEM micrographs of region 1 lift-out from the precrack dimples of wrought Ti-811 in Fig. 2b. (a) Low magnification overview at $g = [0002]$, (b) high magnification image at $g = [0002]$, the white arrowheads indicate two planar slip bands, (c) high magnification image at $g = [01\bar{1}\bar{1}]$, the black arrowhead denotes a grain boundary at bottom right corner. $B = [2\bar{1}\bar{1}0]$, and in all cases black arrows indicate the excited g vector.

the $\langle c + a \rangle$ slip will be preferentially activated in region 3.

3.3. Dislocation contrast analysis

After the FIB lift-out experiment, all FIB lamellae were subjected to dislocation contrast analysis, and the same areas in the black dashed boxes were investigated. As shown in Fig. 3a, the c -axis is consistent with the pole figure in region 1 (Fig. 2c). Fig. 3b and c is high magnification images for Fig. 3a. During the dislocation contrast analysis, the electron beam was tilted a few degrees away from the $[2\bar{1}\bar{1}0]$ zone axis to obtain the appropriate g vector. The basal plane was approximately on edge and parallel to the beam direction. The distribution of dislocations seems to be heterogeneous in region 1. Straight dislocation segments were on $(0002)_\alpha$ planes from 600 to 1500 nm beneath the fracture surface (below the Pt deposition) when $g = [01\bar{1}\bar{1}]$ was operating. Most of the straight features were extinct under $g = [0002]$, which suggests that they had a $\langle a \rangle$ type Burgers vector. However, two planar slip bands with a thickness of 20 nm (see white arrowheads in Fig. 3b) remained visible under $g = [0002]$. One explanation is that they are bands of $\langle c + a \rangle$ dislocations, which have contrast under

both $g = [0002]$ and $g = [01\bar{1}\bar{1}]$. However, $\langle c + a \rangle$ type dislocations glide on pyramidal planes, and they are not expected as edge on features residing on the basal plane when the electron beam direction is approximately parallel to $[2\bar{1}\bar{1}0]$. Another possibility is that the two slip bands are residual contrast of $\langle a \rangle$ type edge dislocations. Despite the invisibility criterion $g \cdot b = 0$, the strain field raised from a high density of $\langle a \rangle$ type edge dislocation debris in the bands leads to an incomplete vanished contrast [29]. Therefore, arrays of dislocations including the two slip bands can be determined as $\langle a \rangle$ type dislocations on the basal plane, which is predicted and confirmed by the relative σ_c calculation in Table 1.

The deformed substructure beneath SCC facets (region 2) in wrought Ti-811 is shown in Fig. 4. In Fig. 4a, the black arrowhead at top right corner denotes the secondary crack that is aligned on the basal plane. TEM shows the same crystallographic orientation to the pole figure in Fig. 2f. The bright field (BF) micrograph of Fig. 4a shows a high density of dislocations with $b = \langle c + a \rangle$ under $g = [0002]$, which were not observed in region 1 beneath the dimples (Fig. 3). When $g = [00\bar{1}\bar{1}]$ reflection was excited, localized planar slip bands and straight dislocation segments were observed on the basal plane,

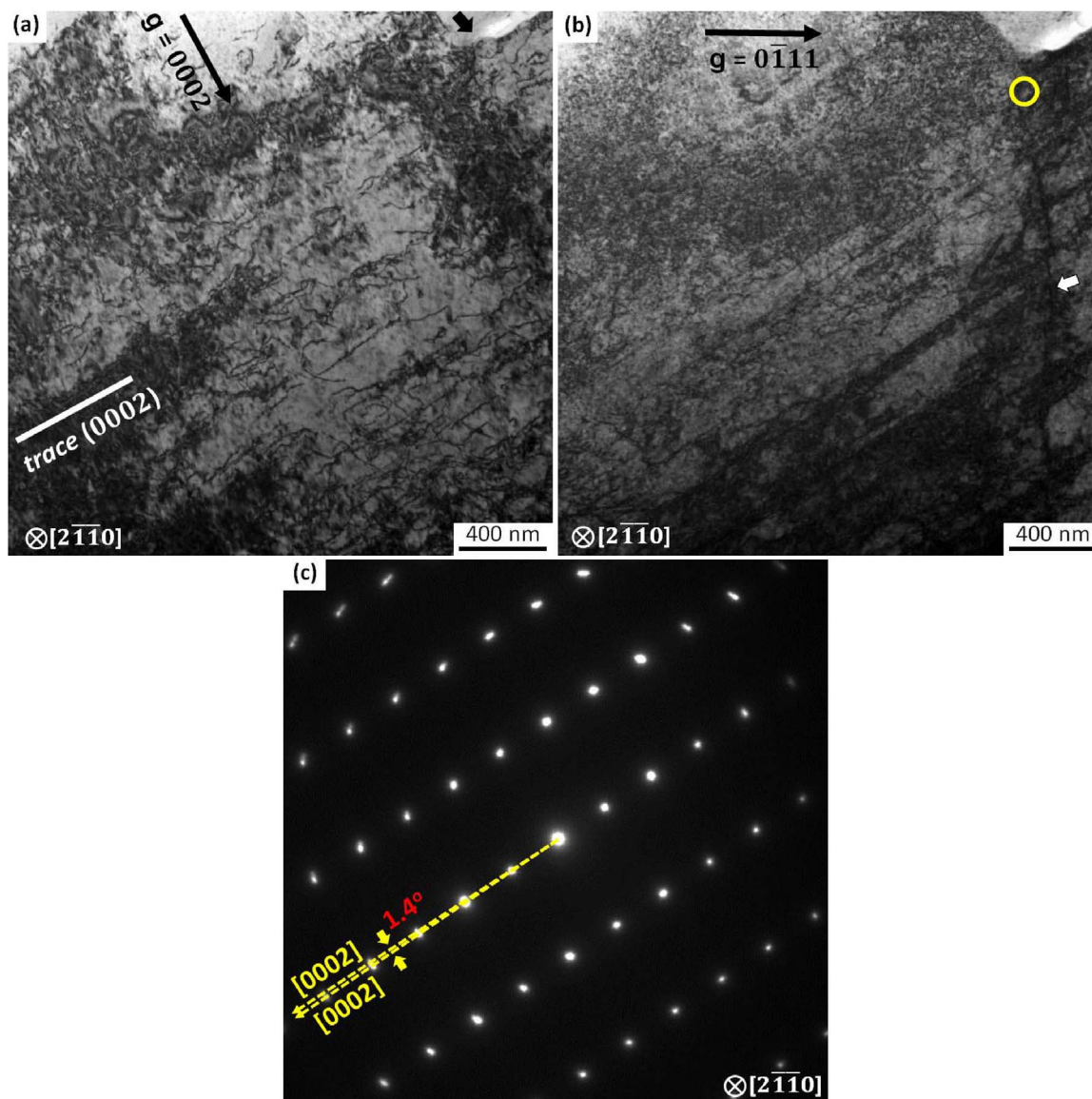


Fig. 4. BF TEM micrographs of region 2 lift-out from the SCC facets of a wrought Ti-811 sample in Fig. 2e. (a) BF image when $g = [0002]$ is excited, the black arrowhead denotes the secondary crack tip which is previously illustrated in Fig. 2e; (b) BF image when $g = [0111]$ is excited, white arrowhead indicates a sub-grain boundary; (c) Selective area diffraction (SAD) pattern taken from the yellow circle in (b). $B \approx [2\bar{1}\bar{1}0]$, and in all cases black arrows indicate the excited g vector.

while dislocations with a $\langle c \rangle$ component were not observed. As the electron beam was close to $[2\bar{1}\bar{1}0]$, the dislocation arrays and bands that resided on the basal plane were determined to be basal $\langle a \rangle$ slip in Fig. 4b. The activation of basal $\langle a \rangle$ slip in region 2 was also predicted by Schmid's law (Table 1). In addition to the predicted basal $\langle a \rangle$ slip, $\langle c + a \rangle$ slip is present in region 2 (Fig. 4a). In Fig. 4b, the feature originating from the secondary crack tip denoted by the white arrowhead was a sub-grain boundary, and grains at each sides of the boundary had a misorientation of 1.4° (Fig. 4c). The small angle sub-grain boundary was not an effective barrier for dislocation motion, therefore the slip bands were continuous across the boundary.

The pre-crack which contained dimples was shorter than the SCC crack which contained facets. As the SCC test was a constant displacement test, the stress intensity factor (K) decreased during crack propagation (increase in crack length), and stress intensity factor was higher in the dimpled region than in the faceted region [1]. However, the number of dislocations in the region beneath the SCC facets was considerably higher than beneath the pre-crack dimples (Figs. 3 and 4). It is to be noted that the foil thickness of these two regions when measured and found to be similar according to Fig. S1 in the

supplementary material. The reasons for such an observation will be discussed in the Section 4.2.

Fig. 5 shows BF images taken with diffraction conditions of $g = [0002]$ and $g =$ in region 3 beneath the faceted fracture of a HIPed Ti-811 sample. Under $g = [0002]_\alpha$ trace beneath the facet containing stair-like steps (black arrowhead in Fig. 5b). In addition to the $\langle a \rangle$ slip, a high density of $\langle c + a \rangle$ entanglements appeared under $g = [0002]$ condition from areas near the facet surfaces to a depth of 1600 nm beneath the facet surfaces (Fig. 5a). Linear $\langle c + a \rangle$ dislocation segments (white arrowheads) were also observed on the $(0002)_\alpha$ plane in both g conditions. In region 3, activation of $\langle c + a \rangle$ slip is predicted by the Schmid's law calculation in Table 1. Fig. 5c is an illustration of stair-like step formation on a faceted fracture surface by the $\langle c + a \rangle$ slip joining the neighbouring basal $\langle a \rangle$ slip bands. This will be discussed in details in the following section.

4. Discussion

To help identify the mechanisms involved in the SCC of Ti-811, the nature and density of dislocations will be discussed in the following

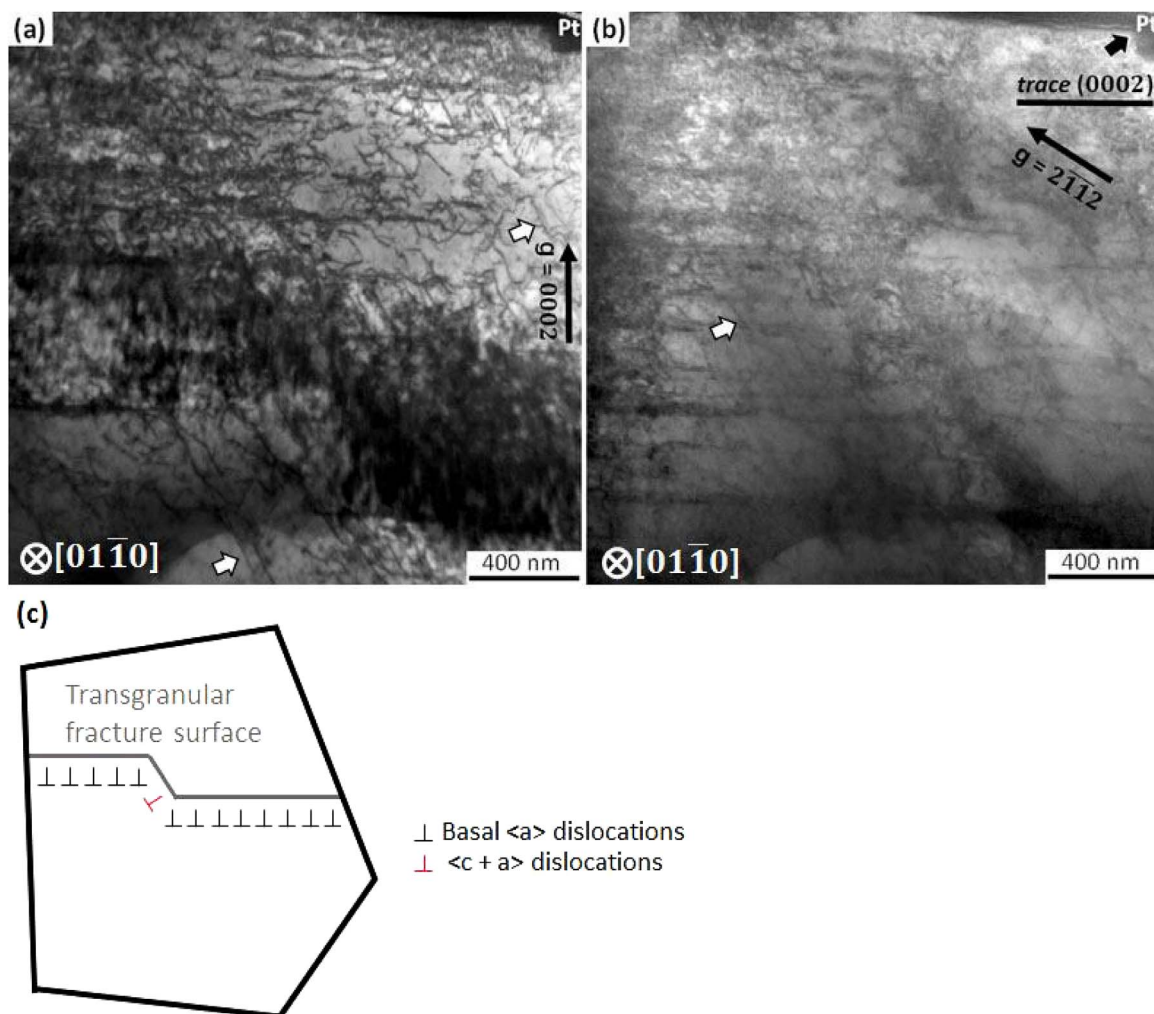


Fig. 5. BF TEM micrographs of region 3 lift-out from the SCC facets of a HIPed Ti-811 sample in Fig. 2 h. (a) $g = [0002]$, (b) $g = [2\bar{1}12]$, (c) a proposed stair-like steps formation mechanism on facets in α -Ti grain. The white arrowheads indicate the linear $\langle c + a \rangle$ segments resided on the $(\bar{2}112)$ plane, and the black arrowhead denotes a stair-like step on facet surfaces. $B \approx [01\bar{1}0]$, and in all cases black arrows represent the excited g vector.

sections. It is possible that they could be affected by the ion beam damage during the FIB lift-out sample preparation stage. Previous studies [30–32] have identified defects, including dislocations, produced by high energy Ga^+ ion damage in FIB lift-out foils. However, a recent study on a near α Ti alloy showed that FIB lamellae, which were prepared by using a sequentially reduced ion beam energy during the thinning process and a final low polishing voltage and current at 2 kV and 28 pA, had a comparable sample quality with electropolished foils in the dislocation contrast experiment [33]. In the current study, a low energy ion beam at 2 kV and 27 pA was used in the final polish process. Therefore, FIB lift-out conducted in our experiment is not expected to affect the dislocation analysis.

4.1. Nature of dislocation

From the TEM contrast analysis, basal $\langle a \rangle$ glides were observed in both regions 1 and 2 (Figs. 3 and 4) from the dimpled and faceted fracture of wrought Ti-811 sample respectively. The activation of such a dislocation type was predicted by the σ_c calculation in Table 1. In addition to the basal $\langle a \rangle$ dislocations, $\langle c + a \rangle$ dislocations were observed only beneath the facets (region 2 in Fig. 4). In general, $\langle c + a \rangle$ glide is important for ductility in α -Ti, which provides the additional independent slip systems for a homogeneous plastic deformation in a HCP crystal based on von Mises criterion [2,34]. Therefore, one would have expected to find $\langle a \rangle$ and $\langle c + a \rangle$ types of

dislocations beneath the ductile dimpled fracture. Instead they were observed beneath SCC facets which are generally thought to indicate brittle fracture.

Dislocation contrast experiment revealed that the basal $\langle a \rangle$ slip bands appeared in both regions 2 and 3 (Figs. 4 and 5) beneath SCC facets regardless of the α -Ti grain orientations. A previous study [1] determined that SCC crack propagated in a “macrozone” containing grains favourably orientated for basal $\langle a \rangle$ slip in a wrought Ti-811 sample. Thus, it seems that basal $\langle a \rangle$ slip is essential for SCC in Ti-811.

Extensive tear ridges and planar slip bands were observed on the SCC facets (Fig. 1d); therefore, the presence of such “facets” alone does not need to be regarded as brittle failure. The tear ridges and planar slip bands are indications of micro-plasticity [8,14,35], which suggests a high degree of dislocation activity around the crack tip. Previous research in Ti-811 proposed that either the basal $\langle a \rangle$ slip or the $\langle c + a \rangle$ slip are promoted in the SCC crack tip region enriched with hydrogen [8].

4.2. Dislocation density

As shown in Figs. 4 and 3, a relatively higher dislocation density was observed beneath the SCC facets (region 2 in Fig. 4) compared to that beneath the dimpled region (region 1 in Fig. 3) for the wrought Ti-811 sample.

The SCC experiment was a constant displacement test [1]. With this test, the stress intensity factor was reduced during SCC crack propagation. The stress intensity factor was much higher in the dimpled region at pre-crack than that during the SCC fracture. It would have been expected that the dislocation density will be higher in region where the stress intensity factor was higher but the opposite was observed. This discrepancy and differences in dislocation however, may reveal some insight into the aqueous NaCl SCC mechanism for Ti-811.

Several studies of hydrogen effects on dislocations have shown that hydrogen lowered the dislocation emission energy [36], and reduced the flow stress and increased dislocation velocity along a narrow slip band [16,36,37]. Another HE study pointed out that hydrogen stabilizes edge components of mixed dislocations and restricts cross slip [37]. These studies [16,36,37], therefore show that hydrogen promotes dislocation emissions and increases dislocation motion on confined crystallographic planes, which results in a high dislocation density, localized slip bands and a macroscopically high crack velocity. The conclusion from all these HE studies are consistent with the experiment observations in the current work where considerably larger amount of dislocations were observed at the SCC faceted region. A high density of localized planar basal $\langle a \rangle$ slip bands and $\langle c + a \rangle$ dislocations was observed below the facets, which suggests hydrogen promoted dislocation emission and movement at the crack tip. Therefore, the aqueous NaCl SCC mechanism of Ti-811 is possibly related to the Absorption Induced Dislocation Emission (AIDE) and Hydrogen Enhanced Localized Plasticity (HELP) mechanisms.

4.3. Hydrogen absorption and diffusion

The SCC mechanism of Ti-811 seems to be related to hydrogen according to the dislocation contrast analysis. Solute hydrogens concentrations were approximately 34 ppm and 24 ppm in the wrought and HIPed Ti-811 samples [1], and they are considered as low concentrations. Therefore, hydrogen could be absorbed from solution at the crack tip in the present SCC study. As described in the previous study [1], hydrogen uptake can be triggered by electrochemical evolution at the crack tip, and the consequent absorption and diffusion into the metal.

Hydrogen is an interstitial element in Ti alloys, and its solubility and diffusivity are much higher in the β phase than in the α phase due to the low pack density of the BCC crystal. As a result, a more rapid diffusion of absorbed hydrogen can be achieved by the interconnected β phase “highway” [10]. In addition, there will be a hydrogen concentration gradient developed around the crack tip during SCC [38]. Following equation is an estimation of the hydrogen diffusion length is [39]:

$$L_H = \sqrt{2D_H t} \quad (2)$$

where t is the diffusion time and D_H is the diffusion coefficient, which is a function of temperature [40]:

$$D_H = D_{H0} \cdot e^{\left(\frac{Q}{RT}\right)} \quad (3)$$

where D_{H0} is the frequency factor, Q is the activation energy and R is the gas constant at 8.314J/(mol.K). As there are no published data of D_{H0} and Q for Ti-811, IMI834 [40] and β -Ti [41] are chosen as the lower and higher reference limits respectively.

Both of Ti-811 and IMI834 are near α Ti alloys, which have a similar β -stabilizer alloying concentration. Fig. 6 shows the microstructure of the reference IMI834 [40] and Ti-811 investigated in this work. The β phase network is discontinuous in lamellae region for the reference IMI834 (Fig. 6a), while both the wrought and HIPed Ti-811 had an interconnected β phase network (Fig. 6b and c). Interconnected β phase increases hydrogen diffusivity, therefore the diffusion coefficient of wrought and HIPed Ti-811 should be higher than the reference of IMI834 [40].

The diffusion coefficient of Ti-811 is expected to be lower than the

bulk diffusion of hydrogen in β -Ti. Because α grains and lamellae in Ti-811 acting as barriers for hydrogen diffusion, which produce a tortuous hydrogen diffusion path.

For IMI834, the reference values are $D_{H0-IMI834} = 274 \times 10^{-9} \text{m}^2/\text{s}$ and $Q = 40.3 \text{kJ/mol}$ [40], and they are $D_{H0-\beta-Ti} = 200 \times 10^{-9} \text{m}^2/\text{s}$ and $Q = 27.8 \text{kJ/mol}$ of BCC β -Ti [41]. Based on Eq. (3), the diffusion coefficient range of Ti-811 is estimated in the range from $D_{H-IMI834}$ is $2.63 \times 10^{-14} \text{m}^2/\text{s}$ to $D_{H-\beta-Ti}$ is $2.89 \times 10^{-12} \text{m}^2/\text{s}$ at room temperature (300 K).

The bulk hydrogen diffusion rate (diffusion length/time) of Ti-811 is then calculated by Eq. (2). The estimation is in the range between $2.30 \times 10^{-7} \text{m/s}$ ($L_{H-IMI834}$) and $2.40 \times 10^{-6} \text{m/s}$ ($L_{H-\beta-Ti}$). As the plateau SCC crack velocity was in the order of 10^{-5}m/s in the previous study [1], which is at least one magnitude higher than the calculated hydrogen diffusion rate range. This determines that bulk hydrogen diffusion is not sufficient for hydrogen related SCC mechanisms operating in a high crack velocity case.

Nevertheless, hydrogen diffusivity can be promoted by transportation through dislocations movement [42], especially in the presence of planar slip bands which allow for a longer rapid diffusion route [43]. Hydrogen transport through slip bands has been reported in various systems including steels [44], Al [43], and Ti [45]. It was determined that the pipe diffusion along dislocation was kinetically preferred than volume diffusion, and that the hydrogen diffusion rate was increased by orders of magnitude through the pipe diffusion [42,43]. The coherent ordered α_2 precipitates lead to localized planar slip bands with a length longer than 2 μm beneath SCC facets (Fig. 4b and Fig. 5b). These planar slip bands present a directional transport highway for the absorbed hydrogen at crack tip to diffuse into grain interior. As calculated in the above paragraphs, the SCC crack velocity was at least one magnitude higher than the bulk hydrogen diffusion rate in Ti-811. Therefore, hydrogen transport through slip bands should be the diffusion method for the situation of high SCC crack velocity. In addition to hydrogen segregation and diffusion, the hydrogen concentration is high within the slip bands, which would lead to easier crack propagation along the slip bands [2].

4.4. Crystallographic orientations of SCC faceted planes

In Ti-811, SCC fracture planes were reported to be close to $(0002)_\alpha$ plane [8,14,46,47], and they were inclined 5° to 15° away from the basal plane [8]. Coincidentally, a well-known hydride habit plane $\{10\bar{1}7\}_\alpha$ is approximately 15° away from the $(0002)_\alpha$ plane [8,14]. As previously reviewed in the introduction, the hydride formation and fracture mechanism was not considered suitable for SCC in Ti-811.

In the current study, three regions (2, 3, and 4 in Fig. 2) were examined beneath the SCC facets on the wrought and HIPed Ti-811 samples. The faceted fracture plane of regions 2 and 3 was parallel to $(0002)_\alpha$, which are illustrated in Figs. 4 and 5. Especially for region 2, a secondary crack was also observed on the basal plane. Fig. 7 shows a facet formed on a plane inclined approximately 15° away from the basal plane in region 4, which is close to a hydride habit plane $\{10\bar{1}7\}_\alpha$ [8,14]. In this study, hydride was not observed during the fractography and TEM examinations. Beneath the facet, a high density of $\langle c + a \rangle$ entanglements appear as shown in Fig. 7. The irrational $\{10\bar{1}7\}_\alpha$ planes are incapable of slip, the mechanism of facet formation on $\{10\bar{1}7\}_\alpha$ planes is still unidentified.

The direct observations (regions 2, 3, and 4) showed that facet formations were on crystallographic planes either parallel to, or inclined 15° away from the basal plane. These observations are inconsistent with the range of 5° to 15° away from the basal plane in the previous study [8]. The method of quantitative tilt fractography/EBSD measures the average crystallographic orientation of facets with an inaccuracy of $\pm 3^\circ$ [8,14], while TEM images of the FIB lift-out foils showed direct orientations. The average measurements on facets with those ductile features, including planar slip bands and tear ridges, may

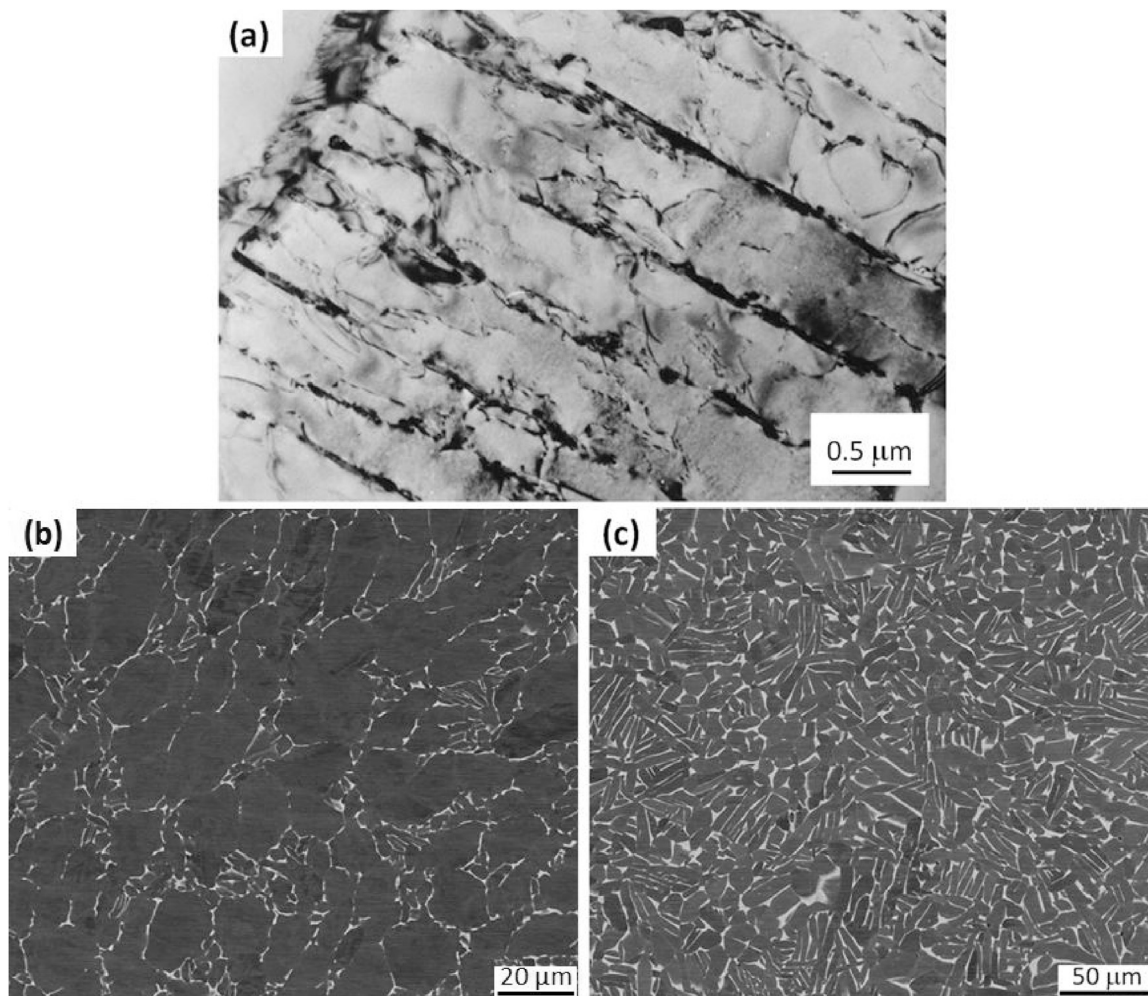


Fig. 6. (a) TEM image of the fully lamellar IMI834 alloy in the study of [40], (b) BSE SEM image of the wrought Ti-8Al-1Mo-1 V alloy with a bi-modal microstructure used in the current study, (c) BSE SEM image of the HIPed Ti-8Al-1Mo-1 V alloy used in the current study [1].

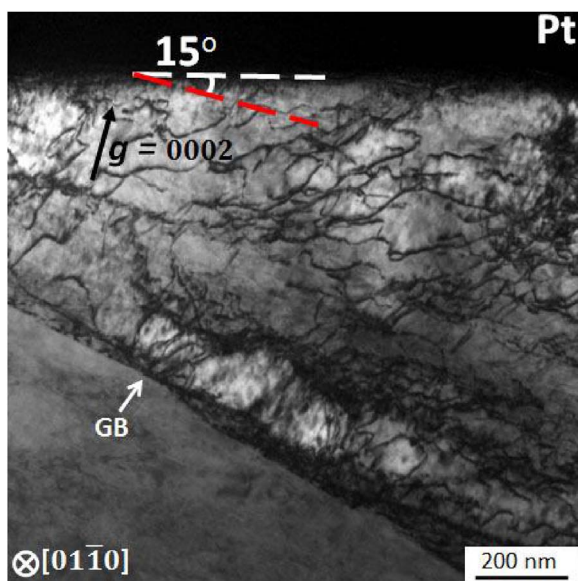


Fig. 7. BF TEM micrograph of region 4 lift-out from the SCC facets of HIPed Ti-811 sample in Fig. 2 h. $g = [0002]$, $B \approx [01\bar{1}0]$. The white dashed line denotes the faceted surface and the red dashed line is the $(0002)_\alpha$ trace. The black arrow indicates the excited g vector.

have contributed to the inconsistency.

The orientation of facets is related to the operating dislocation systems beneath. For regions 2 and 3, faceted planes on $(0002)_\alpha$ could be a result of the fracture propagation along the basal $\langle a \rangle$ slip bands. A slight difference is that the facet surfaces contained stair-like steps formed by joining adjacent basal $\langle a \rangle$ slip bands observed in region 3 (Fig. 5).

4.5. SCC mechanism

The tear ridges on facets indicated a high degree of dislocation activity at the crack tip. A previous study [8] proposed a hypothesis, in which either basal $\langle a \rangle$ slip or $\langle c + a \rangle$ slip were encouraged by hydrogen at the crack tip, and the present work provides the first direct TEM evidence that this is likely the case.

The ductile features of stair-like steps with a spacing at 700 nm on the facet of region 3 (Figs. 2 h and 5) were related to the planar slip bands on facets (Fig. 1d). These steps indicate highly localized plastic deformation. According to the dislocation contrast analysis in Fig. 5, extensive basal $\langle a \rangle$ slip bands, and pyramidal $\langle c + a \rangle$ dislocations were observed beneath the facets. As these steps are parallel to the $(0002)_\alpha$ plane, it suggests that the stair-like step formation was a result of $\langle c + a \rangle$ dislocations joining neighbouring basal $\langle a \rangle$ slip bands in Fig. 5c.

In SCC of Ti alloys, the pH was found to be below 2 at the crack-tip zone for a neutral bulk solution [9]. The low pH value (high hydrogen ion concentration) is a result of anodic reaction of Ti, and hydrolysis of

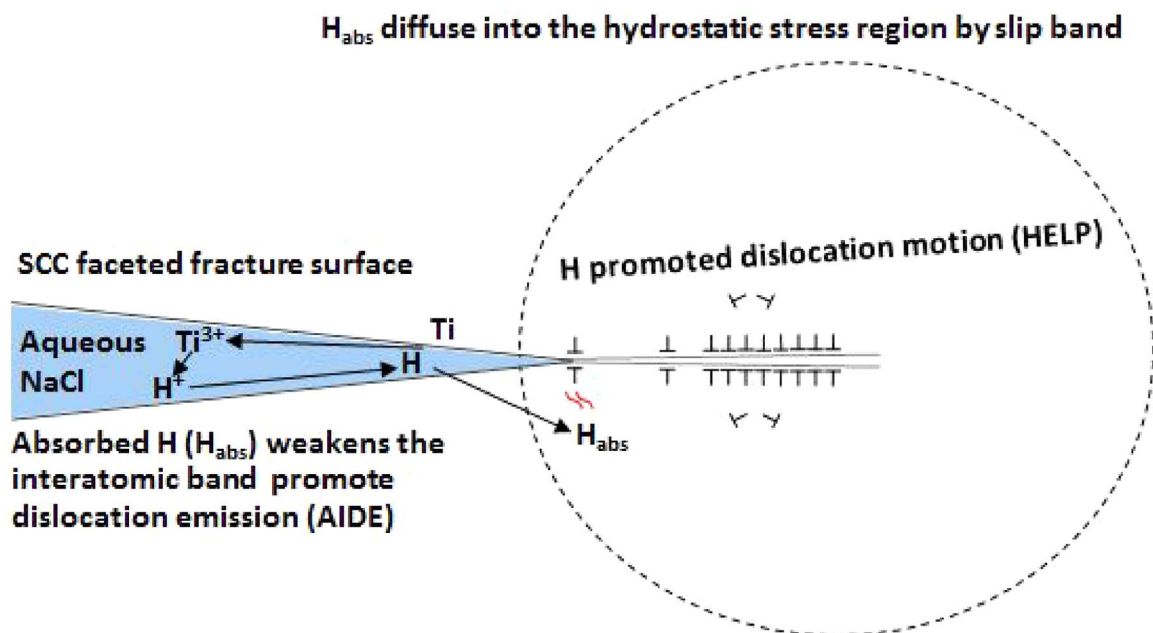


Fig. 8. Illustration of a combined SCC mechanism including Absorption Induced Dislocation Emission (AIDE) and Hydrogen Enhanced Localized Plasticity (HELP) for aqueous NaCl SCC in Ti-8Al-1Mo-1 V. H_{abs} is the absorbed hydrogen.

Ti ions at the crack-tip zone [9]. Then, H atoms are evolved and absorbed at the crack tip. Therefore, the absorbed hydrogen weakens the interatomic band, promotes dislocation emission and increases the dislocation density around the crack tip by AIDE. The diffused hydrogen then promoted a localized plastic deformation ahead of the crack tip by HELP. The overall crack propagation was a result of the accumulation of highly localized plastic deformation in the vicinity grains ahead of the crack tip. Thus, a combined AIDE and HELP mechanism schematically shown in Fig. 8 is proposed for the SCC of $\alpha + \beta$ Ti alloys in aqueous NaCl solution.

5. Conclusions

FIB lift-out, T-EBSD, and dislocation contrast analysis were applied to study the dislocation substructure of α grains beneath pre-crack dimples and SCC facets in Ti-811. The conclusions are: A dislocation type change was observed in the pre-crack dimpled region and SCC faceted region. Both grains were orientated favourably for basal $\langle a \rangle$ slip. Basal $\langle a \rangle$ slip was the only system activated beneath dimples, while basal $\langle a \rangle$ and $\langle c + a \rangle$ slip were observed beneath SCC facets.

i. An increase in dislocation density was observed in the SCC faceted region compared to that of the pre-crack dimples. The increased dislocation density is an evidence of micro-plasticity related to AIDE mechanism around the crack tip.

ii. The crystallographic planes of the SCC facets were either parallel to, or inclined 15° away to the (0002) _{α} plane. The orientation of facets parallel to the basal plane is attributed to the operating dislocations beneath.

iii. The main hydrogen source is likely external absorbed hydrogen from the solution at the crack tip rather than solute hydrogen. Subsequent hydrogen diffusion is not solely dependent on bulk diffusion, but rather on pipe diffusion through the planar slip bands in α -Ti grains ahead of SCC crack tip.

iv. A combined AIDE and HELP mechanism is proposed as the aqueous NaCl SCC mechanism for $\alpha + \beta$ Ti alloys.

Conflict of interest

The authors declare no competing financial interest.

Funding

This research did not receive any specific grant from funding agencies in the public, commercial, or not-for-profit sectors.

Acknowledgements

Sheng Cao was supported by Australian Postgraduate Awards (APA) and International Postgraduate Research Scholarship (IPRS) for his PhD study. The technical support from Monash Centre of Electron Microscopy (MCEM) and Monash Centre of Additive manufacturing (MCAM) is acknowledged. The authors appreciate the helpful discussions with Dr. Xi-Ya Fang, Dr. Jisheng Ma and Mr. Yu Zhang.

Appendix A. Supplementary data

Supplementary data associated with this article can be found, in the online version, at <http://dx.doi.org/10.1016/j.corsci.2017.05.025>.

References

- [1] S. Cao, C.V.S. Lim, B. Hinton, X. Wu, Effects of microtexture and Ti3Al (β) precipitates on stress-corrosion cracking properties of a Ti-8Al-1Mo-1 V alloy, *Corros. Sci.* 116 (2017) 22–33, <http://dx.doi.org/10.1016/j.corsci.2016.12.012>.
- [2] G. Lütjering, J.C. Williams, *Titanium*, 2nd ed., Springer, Berlin, 2007, <http://dx.doi.org/10.1007/978-3-540-73036-1>.
- [3] R.R. Boyer, G. Welsch, E.W. Collings, *Materials Properties Handbook – Titanium Alloys*, ASM, International, Materials Park, OH, 1994, https://app.knovel.com/web/toc.v/cid:kpMPHTA002/viewerType:toc/root_slug:materials-properties.
- [4] G. Wang, Z. Chen, J. Li, J. Liu, Q. Wang, R. Yang, Microstructure and mechanical properties of electron beam welded titanium alloy Ti-6246, *J. Mater. Sci. Technol.* (2016), <http://dx.doi.org/10.1016/j.jmst.2016.10.007>.
- [5] N. Ao, D. Liu, S. Wang, Q. Zhao, X. Zhang, M. Zhang, Microstructure and tribological behavior of a TiO₂/hBN composite ceramic coating formed via micro-arc oxidation of Ti-6Al-4 V alloy, *J. Mater. Sci. Technol.* 32 (2016) 1071–1076, <http://dx.doi.org/10.1016/j.jmst.2016.06.015>.
- [6] R.R. Boyer, *Titanium and its alloys: metallurgy, heat treatment and alloy characteristics*, *Encycl. Aerosp. Eng.* (2010) 1–12, <http://dx.doi.org/10.1002/9780470686652.eae198>.
- [7] M. Atapour, A.L. Pilchak, M. Shamanian, M.H. Fathi, Corrosion behavior of Ti-8Al-1Mo-1V alloy compared to Ti-6Al-4 V, *Mater. Des.* 32 (2011) 1692–1696, <http://dx.doi.org/10.1016/j.matdes.2010.09.009>.
- [8] A.L. Pilchak, A.H. Young, J.C. Williams, Stress corrosion cracking facet crystallography of Ti-8Al-1Mo-1V, *Corros. Sci.* 52 (2010) 3287–3296, <http://dx.doi.org/10.1016/j.corsci.2010.05.046>.

- [9] R.J.H. Wanhill, Aqueous stress corrosion in titanium alloys, *Br. Corros. J.* 10 (1975) 69–78 <http://www.scopus.com/inward/record.url?eid=2-s2.0-0016628255&partnerID=40&md5=2557f8ad4cfd65eb2d90a23a6b318a47>.
- [10] I. Chatteraj, Stress corrosion cracking (SCC) and hydrogen-assisted cracking in titanium alloys, in: V.S. Raja, T. Shoji (Eds.), *Stress Corros. Crack. Theory Pract.*, 2011 Woodhead Publishing, Cambridge, 2016, pp. 381–408, <http://dx.doi.org/10.1533/9780857093769.3.381>.
- [11] C. Leyens, M. Peters, *Titanium and Titanium Alloys*, Wiley-VCH, Weinheim, 2003, <http://dx.doi.org/10.1002/3527602119>.
- [12] J.C. Williams, A.W. Sommer, P.P. Tung, The influence of oxygen concentration on the internal stress and dislocation arrangements in α titanium, *Metall. Trans.* 3 (1972) 2979–2984, <http://dx.doi.org/10.1007/BF02652870>.
- [13] J.C. Williams, R.G. Baggerly, N.E. Paton, Deformation behavior of HCP Ti-Al alloy single crystals, *Metall. Mater. Trans.* 33 (2002) 837–850, <http://dx.doi.org/10.1007/s11661-002-1016-2>.
- [14] A.L. Pilchak, J.C. Williams, Observations of facet formation in near- α titanium and comments on the role of hydrogen, *Metall. Mater. Trans. A Phys. Metall. Mater. Sci.* 42 (2011) 1000–1027, <http://dx.doi.org/10.1007/s11661-010-0507-9>.
- [15] R.C. Newman, Stress corrosion cracking, in: M. Cottice, R. Graham, S. Lindsay, T. Lyon, D. Richardson (Eds.), *Shreir's Corros. Elsevier*, Oxford, 2010, pp. 864–901, <http://dx.doi.org/10.1016/B978-044452787-5.00035-4>.
- [16] D.S. Shih, I.M. Robertson, H.K. Birnbaum, Hydrogen embrittlement of α titanium: In situ TEM studies, *Acta Mater.* 36 (1988) 111–124.
- [17] J.C. Scully, D.T. Powell, The stress corrosion cracking mechanism of α -titanium alloys at room temperature, *Corros. Sci.* 10 (1970) 719–733, [http://dx.doi.org/10.1016/S0010-938X\(70\)80043-9](http://dx.doi.org/10.1016/S0010-938X(70)80043-9).
- [18] S.P. Lynch, Mechanistic and fractographic aspects of stress-corrosion cracking (SCC), in: V.S. Raja, T. Shoji (Eds.), *Stress Corros. Crack. Theory Pract.* Woodhead Publishing, Cambridge, 2011, pp. 3–89, <http://dx.doi.org/10.1533/9780857093769.1.3>.
- [19] S.P. Lynch, Hydrogen embrittlement (HE) phenomena and mechanisms, in: V.S. Raja, T. Shoji (Eds.), *Stress Corros. Crack. Theory Pract.*, Woodhead Publishing, Cambridge, 2011, pp. 90–130.
- [20] I.M. Robertson, P. Sofronis, A. Nagao, M.L. Martin, S. Wang, D.W. Gross, K.E. Nygren, Hydrogen embrittlement understood, *Metall. Mater. Trans. A Phys. Metall. Mater. Sci.* 46 (2015) 2323–2341, <http://dx.doi.org/10.1007/s11661-015-2836-1>.
- [21] T.P. Chapman, R.J. Chater, E.A. Saunders, A.M. Walker, T.C. Lindley, D. Dye, Environmentally assisted fatigue crack nucleation in Ti-6Al-2Sn-4Zr-6Mo, *Corros. Sci.* 96 (2015) 87–101, <http://dx.doi.org/10.1016/j.corsci.2015.03.013>.
- [22] M. Zhao, Z. Guo, S. Chen, H. Liang, L. Rong, Hydrogen-induced modification in the deformation and fracture of a precipitation-hardened Fe-Ni based austenitic alloy, *J. Mater. Sci. Technol.* 30 (2014) 1155–1159, <http://dx.doi.org/10.1016/j.jmst.2014.03.017>.
- [23] M.D. Pustode, V.S. Raja, N. Paulose, The stress-corrosion cracking susceptibility of near- α titanium alloy IMI 834 in presence of hot salt, *Corros. Sci.* 82 (2014) 191–196, <http://dx.doi.org/10.1016/j.corsci.2014.01.013>.
- [24] R. Gaddam, R. Pederson, M. Hörmqvist, M.-L. Antti, Fatigue crack growth behaviour of forged Ti-6Al-4 V in gaseous hydrogen, *Corros. Sci.* 78 (2014) 378–383, <http://dx.doi.org/10.1016/j.corsci.2013.08.009>.
- [25] A.M. Panindre, V.S. Raja, M. Ajay Krishnan, Explanation for anomalous environmentally assisted cracking behaviour of a wrought Mg-Mn alloy in chloride medium, *Corros. Sci.* 115 (2017) 8–17, <http://dx.doi.org/10.1016/j.corsci.2016.11.001>.
- [26] M.D. Pustode, V.S. Raja, Hot salt stress corrosion cracking behavior of Ti-6242S alloy, *Metall. Mater. Trans. A.* 46 (2015) 6081–6089, <http://dx.doi.org/10.1007/s11661-015-3155-2>.
- [27] N. Cheneau-Späh, J.H. Driver, Plane strain compression of titanium crystals, *Mater. Sci. Forum* 157-162 (1994) 639–644, <http://dx.doi.org/10.4028/www.scientific.net/msf.157-162.639>.
- [28] T.R. Bieler, S.L. Semiatin, The origins of heterogeneous deformation during primary hot working of Ti-6Al-4 V, *Int. J. Plast.* 18 (2002) 1165–1189, [http://dx.doi.org/10.1016/S0749-6419\(01\)00057-2](http://dx.doi.org/10.1016/S0749-6419(01)00057-2).
- [29] M. Wollgarten, M. Beys, K. Urban, H. Liebertz, U. Köster, Direct evidence for plastic deformation of quasicrystals by means of a dislocation mechanism, *Phys. Rev. Lett.* 71 (1993) 549–552, <http://dx.doi.org/10.1103/PhysRevLett.71.549>.
- [30] P.R. Munroe, The application of focused ion beam microscopy in the material sciences, *Mater. Charact.* 60 (2009) 2–13, <http://dx.doi.org/10.1016/j.matchar.2008.11.014>.
- [31] C.A. Volkert, A.M. Minor, Focused ion beam micromachining, *MRS Bull.* 32 (2007) 389–399.
- [32] D. Kiener, C. Motz, M. Rester, M. Jenko, G. Dehm, FIB damage of Cu and possible consequences for miniaturized mechanical tests, *Mater. Sci. Eng. A.* 459 (2007) 262–272, <http://dx.doi.org/10.1016/j.msea.2007.01.046>.
- [33] T.P. Chapman, V.A. Vorontsov, A. Sankaran, D. Rugg, T.C. Lindley, D. Dye, The dislocation mechanism of stress corrosion embrittlement in Ti-6Al-2Sn-4Zr-6Mo, *Metall. Mater. Trans. A* 47 (2016) 282–292, <http://dx.doi.org/10.1007/s11661-015-3181-0>.
- [34] H. Numakura, Y. Minonishi, M. Koiwa, <1123> {1011} slip in titanium polycrystals at room temperature, *Scr. Metall.* 20 (1986) 1581–1586, [http://dx.doi.org/10.1016/0036-9748\(86\)90399-6](http://dx.doi.org/10.1016/0036-9748(86)90399-6).
- [35] A.L. Pilchak, W.J. Porter, R. John, Room temperature fracture processes of a near- α titanium alloy following elevated temperature exposure, *J. Mater. Sci.* 47 (2012) 7235–7253, <http://dx.doi.org/10.1007/s10853-012-6673-y>.
- [36] M.L. Wasz, F.R. Brotzen, R.B. McLellan, A.J. Griffin, Effect of oxygen and hydrogen on mechanical properties of commercial purity titanium, *Int. Mater. Rev.* 41 (1996) 1–12, <http://dx.doi.org/10.1179/095066096790151330>.
- [37] I.M. Robertson, The effect of hydrogen on dislocation dynamics, *Eng. Fract. Mech.* 68 (2001) 671–692.
- [38] I.M. Robertson, H.K. Birnbaum, P. Sofronis, Hydrogen effects on plasticity, in: J.P. Hirth, L. Kubin (Eds.), *Dislocations in Solids*, Elsevier B.V., 2009, pp. 251–293, [http://dx.doi.org/10.1016/S1572-4859\(09\)01504-6](http://dx.doi.org/10.1016/S1572-4859(09)01504-6).
- [39] D. Delafosse, T. Magnin, Hydrogen induced plasticity in stress corrosion cracking of engineering systems, *Eng. Fract. Mech.* 68 (2001) 693–729.
- [40] H.-J. Christ, M. Decker, S. Zeitler, Hydrogen diffusion coefficients in the titanium alloys IMI 834, Ti 10-2-3, Ti 21 S, and alloy C, *Metall. Mater. Trans. A* 31 (2000) 1507–1517, <http://dx.doi.org/10.1007/s11661-000-0161-8>.
- [41] R.J. Wasilewski, *The diffusion of hydrogen, Nitrogen and Oxygen in Titanium*, University, Columbia, 1954.
- [42] J.K. Tien, A.W. Thompson, I.M. Bernstein, R.J. Richards, Hydrogen transport by dislocation, *Metall. Trans. A* 7 (1976) 821–829.
- [43] J. Albrecht, I.M. Bernstein, A.W. Thompson, Evidence for dislocation transport of hydrogen in aluminum, *Metall. Trans. A* 13 (1982) 811–820, <http://dx.doi.org/10.1007/BF02642394>.
- [44] H. Matsunaga, H. Noda, Visualization of hydrogen diffusion in a hydrogen-enhanced fatigue crack growth in type 304 stainless steel, *Metall. Mater. Trans. A* 42 (2011) 2696–2705, <http://dx.doi.org/10.1007/s11661-011-0661-8>.
- [45] C.Q. Chen, S.X. Li, K. Lu, Dislocation interaction with hydrides in titanium containing a low hydrogen concentration, *Philos. Mag.* 84 (2004) 29–43, <http://dx.doi.org/10.1080/14786430310001623533>.
- [46] D.A. Meyn, Analysis of frequency and amplitude effects on corrosion fatigue crack propagation in Ti-8Al-1Mo-1V, *Metall. Trans.* 2 (1971) 853–865.
- [47] J.C. Williams, M.J. Blackburn, A comparison of phase transformations in three commercial titanium alloys, *ASM Trans. Q.* 60 (1967) 373–383.